Supplementary Information

Photothermal-Stable Pure-Iodide Wide-Bandgap Perovskite Solar Cells with Suppressed Ionic Losses

Ziwei Liu[a], Qifan Feng[a], Nikhil Kalasariya[a], Zhaoyu Lou[a], Shuo Zhang[b], Xiaofeng Chen[b], Weizhong Zheng[b], Xiaofeng Huang[c], Dewei Zhao[d], Yongzhen Wu[b], Martin Stolterfoht[a,*]

[a]Electronic Engineering Department, The Chinese University of Hong Kong, Shatin, N.T, Hong Kong 999077, China,mstolterfoht@ee.cuhk.edu.hk
[b]School of Chemistry and Molecular Engineering, East China University of Science and Technology, Shanghai 200237, China
[c]Department of Materials Science & Engineering, City University of Hong Kong, Kowloon, Hong Kong 999077, China.
[d]College of Materials Science and Engineering & Institute of New Energy and Low-Carbon Technology & Engineering Research Center of Alternative Energy Materials and Devices, Ministry of Education, Sichuan University, Chengdu 61065, China.

EXPERIMENTAL PROCEDURES

Materials

Cesium iodide (CsI), formamidinium iodide (FAI), methylammonium iodide (MAI), dimethylammonium iodide (DMAI), lead iodide (PbI_2), and lead bromide ($PbBr_2$) were purchased from TCI. All solvents, including N,N-dimethylformamide (DMF), Dimethyl sulfoxide (DMSO), N-methyl-2-pyrrolidone (NMP), isopropanol (IPA), Anisole, and methyl acetate, were obtained from Sigma-Aldrich. The self-assembled monolayer (SAM), passivation materials ($EDAI_2$ and PDI), crystallization additives (MACl, PMAI, and $Pb(SCN)_2$), as well as Fullerene (C_{60}) and bathocuproine (BCP), Nickel oxide (NiO_x) was purchased from Xian YuRi Solar Energy Technology Co., Ltd.

Perovskite fabrication:

1.2 M precursor solutions were prepared in DMF-based solvents. For 77:23 Br–I, 800 µL DMF: 200 µL DMSO (v/v = 4:1) were used; for pure-iodide, 800 µL DMF: 200 µL NMP (4:1). Solutions were stirred overnight at room temperature. Films were spin-coated at 3,000 rpm for 40 s; at 25 s, an anti-solvent was dripped (200 µL anisole for Br–I; 50 µL methyl acetate for pure-I). All films were annealed at 100 °C for 10 min.

Interfacial modification

ITO substrates were ultrasonically cleaned (DI water → acetone → IPA) and treated by UV (30 min). Aqueous NiO_x (20 mg mL^{-1}) was spin-coated (3,000 rpm, 30 s) and annealed (120 °C, 10 min). A self-assembled monolayer (SAM, 1 mg mL^{-1} in IPA) was then deposited under the same spin conditions and annealed (100 °C, 10 min). After perovskite deposition, surface passivation was applied in two steps: $EDAI_2$ (0.5 mg mL^{-1} in IPA) and PDI (0.2 mg mL^{-1} in IPA), each at 3000 rpm, 30 s, followed by 100 °C, 5 min anneal.

Based on the literature, we expect that $EDAI_2$ primarily repairs under-coordinated Pb sites and halide vacancies at the top surface/perovskite-C_{60} contact, forming a compact hydrogen-bonded layer that suppresses interfacial non-radiative recombination.24 In addition, PI has been shown to form a dipole that realigns the perovskite and C_{60} energy levels. Although we note that in this study, no improvement of the neat perovskite layer was observed in contrast to our results where the neat material improves considerably, suggesting an additional passivation effect. has been shown that PDI resides predominantly in molecular form at the surface (rather than forming 2D phases), suppresses deep-level defect formation via acid-base inhibition of A-site deprotonation, and partially penetrates C_{60} to promote favorable interfacial band bending, facilitating charge extraction.

Additive engineering

For 77:23 Br–I, the precursor contained 10 mol% PMAI and 1 mol% $Pb(SCN)_2$.

For pure-iodide, the precursor contained 10 mol% MACl, 10 mol% PMAI, and 1 mol% $Pb(SCN)_2$.

Characterization:

Current Density–Voltage *(J–V)* Characterization:

J–V curves were recorded using a Keithley 2400 source meter operated in a 2-wire source-measure mode. The light source employed was an Oriel AAA solar simulator equipped with a Xenon lamp, delivering AM1.5G illumination at an intensity close to 100 mW/cm². A calibrated Si photodiode was used to monitor the light intensity during measurements continuously. The exact illumination level was used to determine device efficiencies, and the system was calibrated with a KG3-filtered silicon reference cell certified by Fraunhofer ISE. All measurements were conducted at a controlled temperature of 25°C, and the voltage was swept at a scan rate of 100 mV/s. *J–V* curves at different voltage scan rates and pre-conditioning conditions were explored in this work.

Photoluminescence (PL) Spectroscopy:

Absolute PL spectra were collected using an AVANTES SenseLine ULS2048×64 spectrometer. The excitation source was a 405 nm laser. Absolute PL spectra were collected using an AVANTES SenseLine ULS2048×64 spectrometer. The excitation source was a 405 nm laser. All PL measurements were performed on glass–glass encapsulated samples prepared in an N_2-filled glovebox, and PL was used to assess non-radiative recombination losses.

Calculation of the quasi-Fermi level splitting (QFLS)

We calculated the internal electron-hole Quasi-Fermi Level Splitting (QFLS) from PLQY results, employing the following equation:

$$\mathrm{QFLS} = k_B \times \ln\left(\mathrm{PLQY} \times J_\mathrm{G}/J_0^{\mathrm{rad}}\right)$$

where J_G is the generated current density at 1 sun illumination, approximated as the short-circuit current density of the complete solar cell. J_0^{rad} is the radiative recombination current in the dark. We note that in the case of halide segregation, the pure-iodine phase (which does not correspond to the bandgap) was disregarded for the calculation of the PLQY as discussed in the main text.

Time-of-Flight Secondary Ion Mass Spectrometry (TOF-SIMS):

TOF-SIMS was employed to perform depth-resolved compositional analysis of halide ion distributions in perovskite layers. A pulsed ion beam (e.g., Bi^+ or Cs^+) was used to bombard the film surface, and secondary ions were collected. The resulting depth profiles of Br^- and I^- ions revealed compositional gradients and interface enrichment phenomena, enabling the correlation of ion redistribution with observed changes in device performance and electric field structure.

Capacitance–Frequency (*C–f*) Measurements:

C–f analysis was carried out to assess the ionic and dielectric responses within the devices under different aging conditions using the FastChar setup developed by SolarSense Technologies Ltd. Capacitance was collected by applying a small AC perturbation (typically 50 mV) across a wide frequency range (1 Hz to 1 MHz) in the dark at room temperature. The measurements help distinguish between geometric capacitance, interface accumulation, and slow ionic relaxation processes, providing additional insights into field screening and charge storage behavior within the perovskite layer.

Bias-Assisted Charge Extraction (BACE):

To evaluate slow-moving ionic and capacitive charges in the device, BACE measurements were conducted in the dark using the FastChar setup developed by SolarSense Technologies Ltd. The procedure began by biasing the device at a pre-conditioning voltage (V_{pre}) close to V_{OC}, allowing photo-injected charges to equilibrate with the steady-state short-circuit current. During BACE acquisition, the stressor, either illumination of the heart was switched off, and BACE was measured in the dark at room temperature. After a specified delay time (typically 5 times the charge extraction duration), the device was switched to a collection voltage (V_{coll} = 0V), prompting the extraction of accumulated electronic and ionic charges. Delay durations ranged from 5 s to 10 s to ensure complete redistribution of ionic species across the active layer.

Fast-Hysteresis and Current Decay Analysis:

Rapid J–V scans were acquired using the FastChar setup developed by SolarSense Technologies Ltd. by initially biasing the device slightly above its open-circuit voltage (V_{OC}), followed by applying a triangular voltage waveform ranging from V_{OC} to −0.1 V and back to Voc. The frequency or scan rate of this voltage ramp was controlled using a function generator. The pre-bias holding time at V_{OC} was maintained at five times the total duration of the voltage sweep. During the scan, the resulting current response was captured using an oscilloscope. The *J-V* scan at slow scan speeds with the FastChar setup matches those obtained with a Keithley SMU.

Photothermal MPPT

The temperature of the cell was set by placing it inside a metallic sample holder on a hotplate at 85°C. We further confirmed that the sample holder exhibits the same temperature on all sides enclosing the cell.

Ab Initio Molecular Dynamics Simulations:

Ab initio molecular dynamics simulations (AIMD) were performed with the CP2K package in canonical (NVT) ensemble. The PBE-D3 functional was used with double-zeta basis sets (DZVP-MOLOPT-SR) and Goedecker–Teter–Hutter pseudopotentials.[1,2] Build two defect-free models, namely $MAPbI_3$ and $Cs_{0.3}DMA_{0.2}MA_{0.5}PbI_3$, and two VI models namely defect-$MAPbI_3$ and defect-$Cs_{0.3}DMA_{0.2}MA_{0.5}PbI_3$. The time step was set to 0.5 fs with the temperature controlled using Nosé–Hoover thermostat [3] at 358 K. The AIMD simulations were run for approximately 80 ps.

DFT Simulations:

Calculations were performed within the DFT framework as implemented in Vienna Ab Initio Simulation Package (VASP) with the projected augmented wave (PAW) pseudopotential.[4,5] The generalized gradient approximation with the Perdew–Burke–Ernzerhof (PBE) functional was employed to describe exchange and correlation effects.[6] DFT-D3 method was used for the van der Waals (vdW) correction. The plane-wave cutoff energy was 520 eV. The energy and force convergence criteria were set to 10-6 and 0.05 eV·Å-1, respectively. The Brillouin zone was sampled with Γ-centred k-mesh densities of more than $2\pi \times 0.02$ Å-1 for geometry optimization and energy-related calculations. Models of surface I vacancy defects (initial positions) and internal I ions migrating to these vacancies (final positions) were constructed for $MAPbI_3$ and $Cs_{0.3}DMA_{0.2}MA_{0.5}PbI_3$, respectively. Subsequently, the ion migration path models were generated by utilizing the nebmake.pl script that comes with the VTST, and calculations were carried out using the Climbing Image Nudged Elastic Band (CI-NEB) method.[7] The final structure was illustrated with VESTA software.[8]

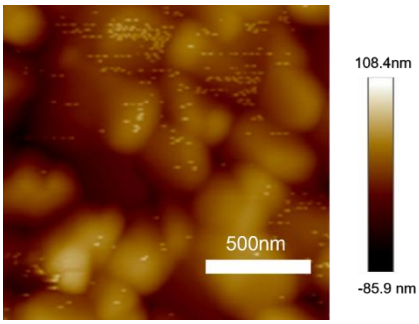

Figure S1. AFM image of the 77:23 Br–I perovskite film.

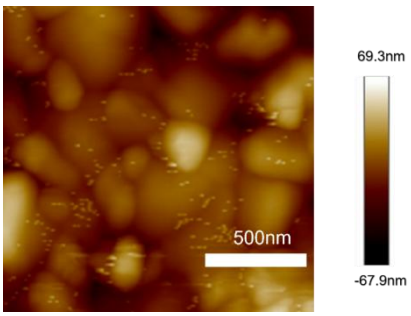

Figure S2. AFM image of the pure iodide perovskite film.

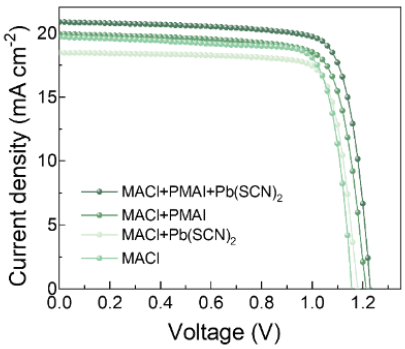

Figure S3. Reverse *J–V* curves of pure iodide devices with different additive combinations (without passivation).

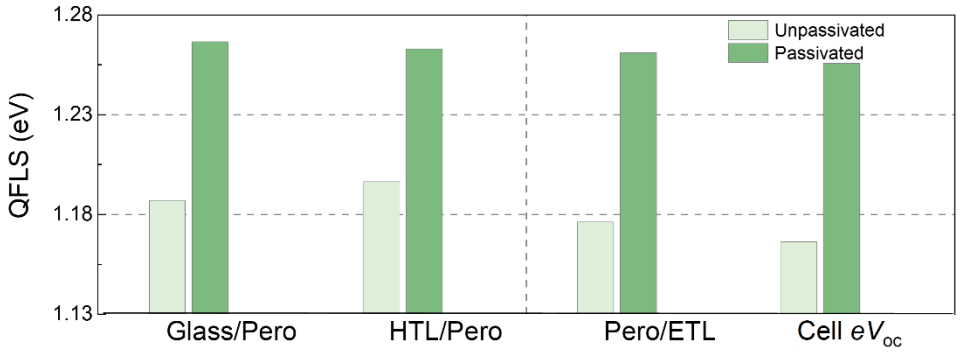

Figure S4. QFLS of the control and dual-passivated films of pure iodide.

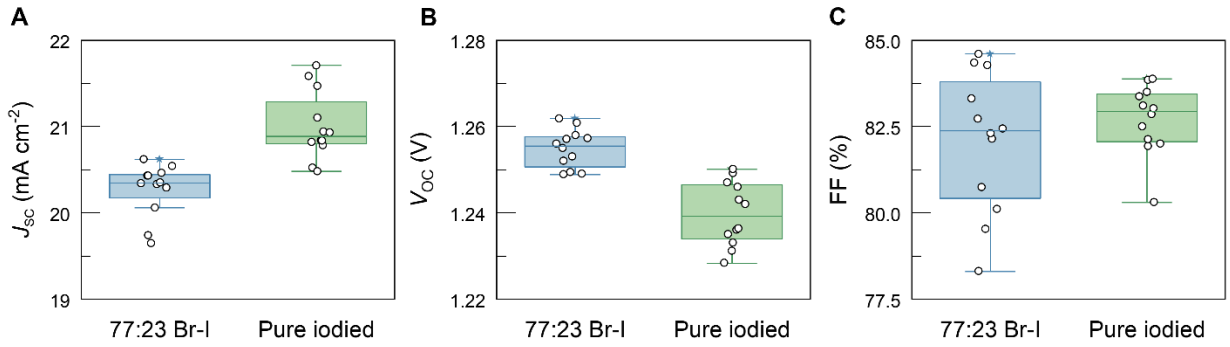

Figure S5. Statistical distribution of the PCE parameters. (A) J_{sc} (B) V_{oc} (C) FF.

天津市计量监督检测科学研究院

Tianjin Institute of Metrological Supervision and Testing

检测报告

Test Report

报告编号：JLY20251005W　　共 4 页　第 4 页

Report No.　　Page No.4-4

检 测 项 目 及 结 果

检测项目 Test Item	光伏电流-电压特性 I-V Characteristic							
测试时间 Date	2025.10.27							
测试条件 Condition	使用稳态 AAA 级太阳模拟器，在 AM1.5G，1000W/m^2，25.0℃条件下测试 Sample was tested under the condition of AM1.5G, 1000W/m^2, 25.0℃ with a steady-state class calibrated AAA solar simulator							
有效面积 Active area	0.091cm^2 备注：器件的有效面积是由带固定孔径的薄金属掩模板量化。 Remark: Designated area defined by thin metal aperture mask.							
样品编号 №	V_{oc} (V)	I_{sc} (mA)	J_{sc} (mA/cm^2)	P_{max} (mW)	V_{Pmax} (V)	I_{Pmax} (mA)	FF (%)	η (%)
20251005-1	1.256	1.945	21.38	2.014	1.100	1.831	82.46	22.13
测试程序 Test program settings	起始电压：Starting voltage:				-0.10 V			
	终止电压：Termination voltage:				+1.20 V			
	扫描间隔：Scan interval:				0.01 V			
	延迟时间：Delay time:				0.01 s			
I-V 曲线图 *I-V* curve	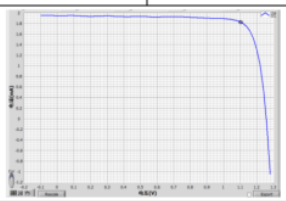							
备注 Remark	—							

————以下空白————

Blank below

Figure S6. Certified *J–V* curve of the champion pure-iodide perovskite solar cell.

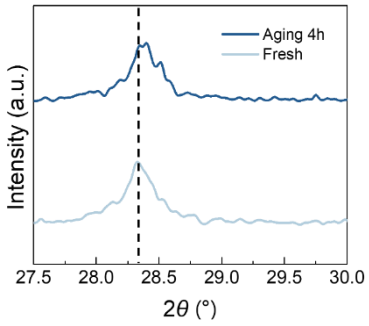

Figure S7. GIXRD patterns (27.5–30°) of 77:23 Br–I perovskite films before and after aging.

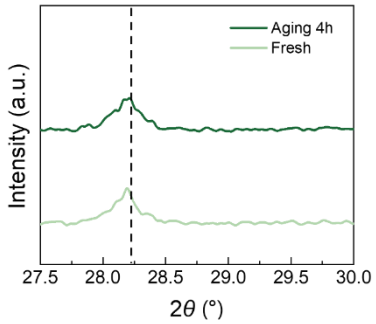

Figure S8. GIXRD patterns (27.5–30°) of pure iodide perovskite films before and after aging.

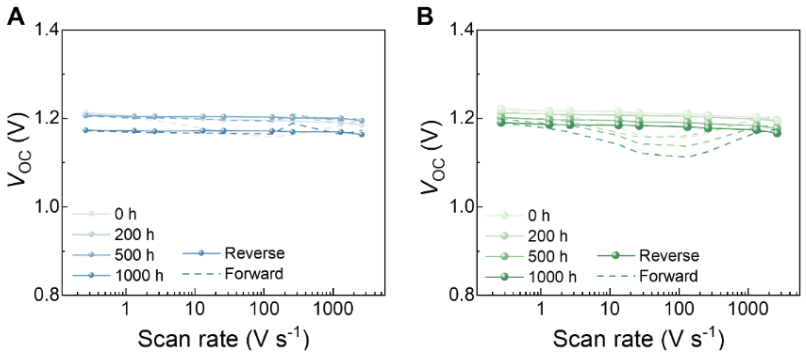

Figure S9. Evolution of open-circuit voltage (V_{OC}) for 77:23 Br–I and pure iodied devices at different light aging (1 sun) stages under various scan rates.

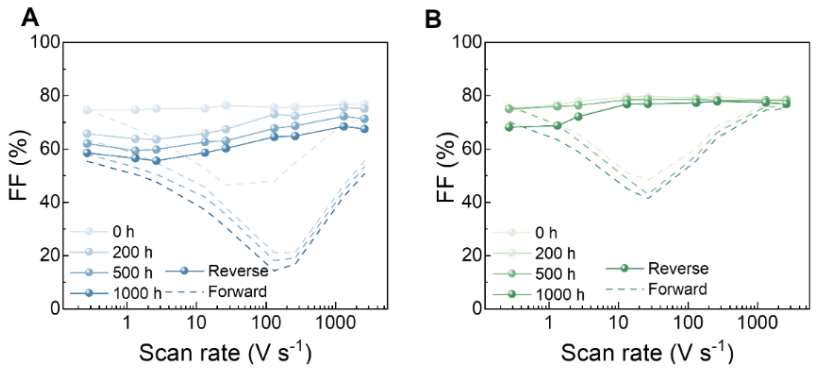

Figure S10. Evolution of fill factors (FF) for 77:23 Br–I and pure iodide devices at different aging (1 sun) stages under various scan rates.

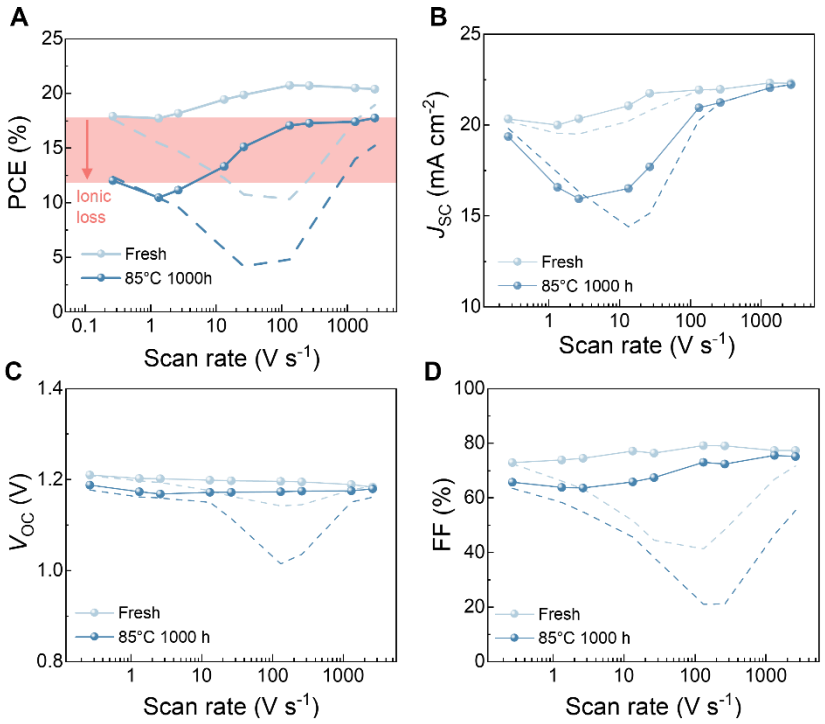

Figure S11. 77:23 Br–I devices' (A) PCE, (B) J_{SC}, (C) V_{OC} and (D) FF obtained from *J-V* characteristics measured at different scan speeds

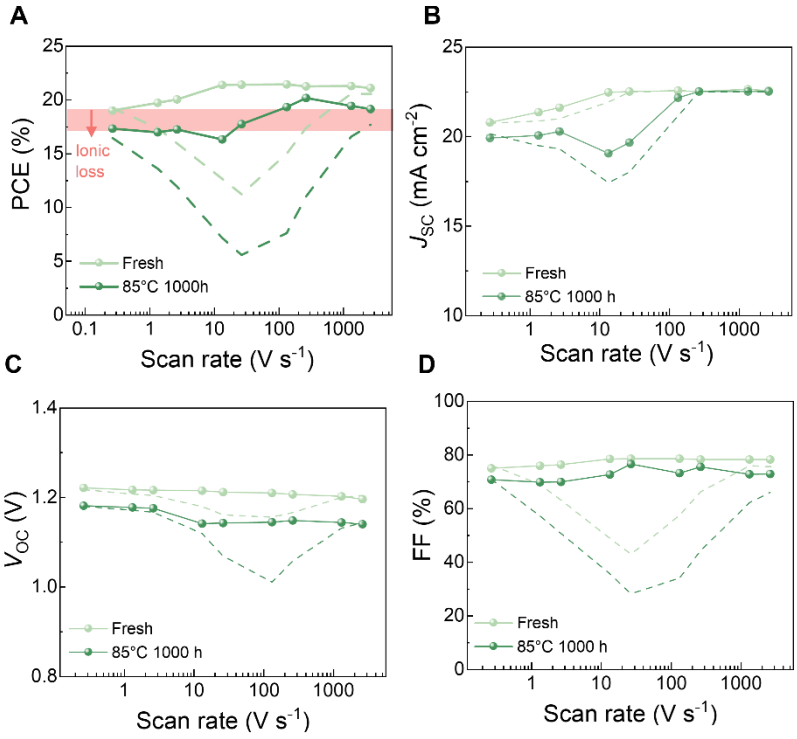

Figure S12. Pure iodide devices' (A)PCE, (B) J_{SC}, (C) V_{OC} and (D) FF obtained from *J-V* characteristics measured at different scan speeds.

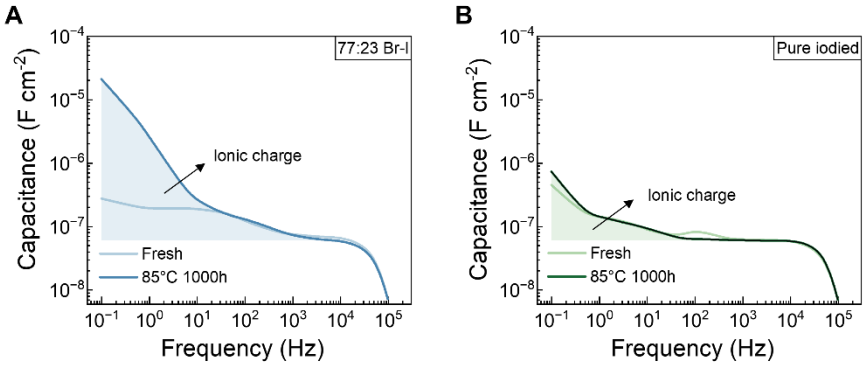

Figure S13. *C-f* response measured before and after aging at 85 °C.

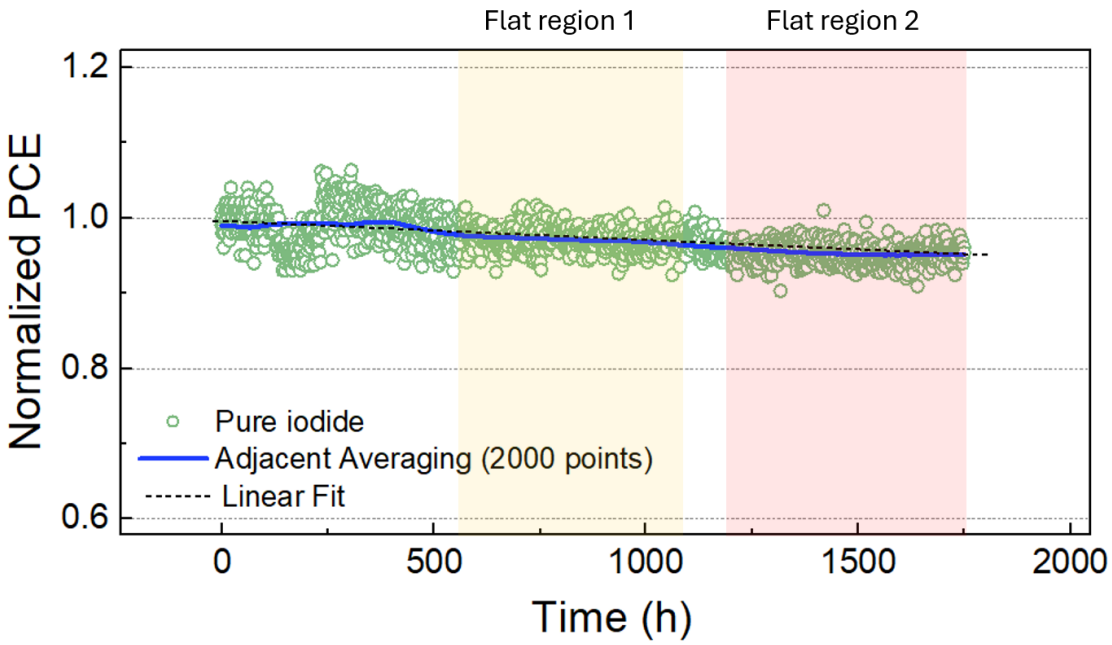

Figure S14. Zoomed photothermal stability evaluated under simultaneous heating (85 °C) and continuous 1-sun illumination using MPPT tracking over extended operation. Highlighted are regions where the decay appears to be flattening (blue fit), which indicates in principle a very long projected lifetime. However, considering that the decay will follow a linear decay (dashed line) results in a more reliable and conservative estimation of the projected T80 lifetime of 8140 h.

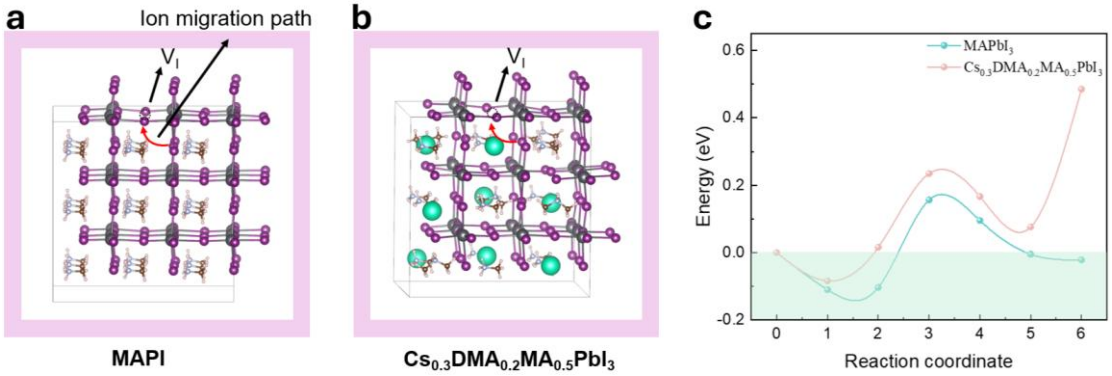

Figure S15. Two ab initio molecular dynamics (AIMD) models of surface I vacancy defects for (A) $MAPbI_3$ and (B) $Cs_{0.3}DMA_{0.2}MA_{0.5}PbI_3$, and a model of internal ions migrating to surface vacancies in 6 equidistant steps along the red arrow. (C) The ion migration energy can quantitatively describe the height of the energy barrier during ion migration and the ease of the migration process. After introducing the A-site cations, the energy barrier for ion migration is increased, making it more difficult for ions to migrate and leading to structural collapse.

Throughout the entire process, the energy values of the $Cs_{0.3}DMA_{0.2}MA_{0.5}PbI_3$ model are considerably higher than those of $MAPbI_3$, indicating that it has a stronger ability to resist ion migration. Especially for jump 6 (where internal ions migrate to the surface and form internal vacancy defects), the energy barrier of $Cs_{0.3}DMA_{0.2}MA_{0.5}PbI_3$ is the highest (~ 500 meV), and it is almost impossible to generate internal halide iodine vacancies (V_I). The energy value of $MAPbI_3$ is less than 0, indicating that it tends to transfer halogen ions from the interior to the exterior, thereby triggering a structural phase transition or collapse. We note that for step 1, the energy values of both models were below 0. Due to the dynamic equilibrium changes of the perovskite structure, there will be a small range of positional movement of the ions. However, for subsequent steps, the energy of $Cs_{0.3}DMA_{0.2}MA_{0.5}PbI_3$ is higher than that of $MAPbI_3$, indicating that the structural fluctuation of the former is less than that of the latter, and is more conducive to maintaining the stability of the structure.

Table S1. Ionic diffusion coefficient (D_{ion}) and ionic loss of 77:23 Br–I and pure iodide perovskites during aging, derived from FH measurements.

Characterization		FH		
Aging time (h)	Ionic loss (%)	Ionic loss (%)	D_{ion} (cm^{-3})	D_{ion} (cm^{-3})
1 sun	77:23 Br-I	Pure iodide	77:23 Br-I	Pure iodide
0	2.59	1.50		
200	7.49	2.10	6.3×10^{-9}	3.1×10^{-9}
500	8.99	2.11		
1000	9.54	2.79		

Table S2. Mobile ion density of 77:23 Br–I and pure iodide perovskites during aging, derived from *C-f* and BACE measurements.

Characterization	*C-f*		BACE	
Aging time (min)	n_{ion} (cm^{-3})	n_{ion} (cm^{-3})	n_{ion} (cm^{-3})	n_{ion} (cm^{-3})
1 sun	77:23 Br-I	Pure iodide	77:23 Br-I	Pure iodide
0	4.3×10^{17}	1.2×10^{17}	3.4×10^{16}	2.3×10^{16}
80	2.3×10^{18}	1.6×10^{17}	5.1×10^{16}	3.0×10^{16}

280	6.0×10^{20}	2.6×10^{17}	6.9×10^{16}	3.2×10^{16}
480	1.7×10^{21}	3.1×10^{17}	2.8×10^{17}	3.3×10^{16}

Table S3. Summary of state-of-the-art reports on the 85°C stability and PCE of perovskite solar cells possessing a bandgap ≥1.67 eV.

PCE (%)	Perovskite Composition	Tempreture (°C)	T_{80} lifetime (h)	Ref.
21.7	$Cs_{0.45}FA_{0.55}Pb(I_{0.85}Br_{0.15})_3$	85	1686	[9]
22.72	$Cs_{0.05}FA_{0.8}MA_{0.15}Pb(I_{0.75}Br_{0.25})_3$	85	423	[10]
23.16	$Cs_{0.05}(FA_{0.77}MA_{0.23})_{0.95}Pb(I_{0.7}Br_{0.3})_3$	85	960	[11]
21.0	$CsI_{0.05}[FA_{0.85}MA_{0.15}Pb(I_{0.85}Br_{0.15})_3]_{0.95}$	85	20	[12]
20.34	FA0.65MA0.20Cs0.15Pb- (I0.8Br0.2)3	85	260	[13]
20.66	Cs0.05MA0.15FA0.8Pb(I0.75Br0.25)3	85	80	[14]
20.3	$FA_{0.65}MA_{0.20}Cs_{0.15}Pb(I_{0.8}Br_{0.2})_3$	85	30	[15]
16.77	FA0.75Cs0.25Pb(I0.8Br0.2)3	85	175	[16]
17.4	$CsPbI_3$	85	5000	[17]
22.48	$Cs_{0.3}DMA_{0.2}MA_{0.5}PbI_3$	85	8140	This work

Supplementary Note S1.

In addition, to estimate the ionic diffusion coefficient, we relate the characteristic ionic response time τ_{ion} to the scan-rate at which the fast hysteresis reaches its maximum. The ionic diffusion coefficient is then approximated by

$$D_{\mathrm{ion}} = \frac{L_{\mathrm{ion}}^2}{\tau_{\mathrm{ion}}}$$

where the ionic characteristic time constant is obtained from the peak-hysteresis condition as

$$\tau_{\mathrm{ion}} = \frac{\Delta V}{S_{\mathrm{peak}}}$$

D_{ion} is the ionic diffusion coefficient $[\mathrm{m}^2\ \mathrm{s}^{-1}]$, τ_{ion} is the ionic characteristic time constant extracted from the scan-rate dependent (fast) hysteresis peak $[\mathrm{s}]$, ΔV is the voltage span used to define the peak hysteresis (typically a half-scan window) $[\mathrm{V}]$, and S_{peak} is the scan rate at which the fast hysteresis is maximal $[\mathrm{V\ s}^{-1}]$.

The characteristic ionic length $L_{\mathrm{ion}}[\mathrm{m}]$ is selected according to the dominant physical picture: $L_{\mathrm{ion}} = w$ in the depletion-dominated case (with w being the depletion width), or $L_{\mathrm{ion}} = \lambda_{\mathrm{D}}$ in the accumulation/Debye-dominated case (with λ_{D} being the Debye length).

Supplementary Note S2.

We note that there is an ongoing discussion regarding the origin of such high low-frequency dark capacitance values at 0V.[18,19] It is also worth noting that, indeed, similar high dark capacitance values of ~10 µF cm^{-2} have been previously explained and reproduced with drift-diffusion (DD) simulations. These models are built upon the simulation framework established by Jacobs et al., which explicitly accounts for 1) high mobile ion density (~1 × 10^{19} cm^{-3}) and 2) the inclusion of surface states (traps) at the perovskite/contact-layer interfaces.[20] These traps enabled the accumulation of a much larger ionic space charge density than would be possible without resorting to unrealistically high contact-layer doping.[20] Finally, we note that under light, often even much higher capacitances were obtained, which were called “giant capacitances”, which could be explained by phase-shifted recombination.[20,21]

Also, the determination of the ion density with BACE does not come without problems, as the formation of zero-field regions after switching to short-circuit conditions should prevent further drift of excess ion densities >> electrode charge, i.e. n_{ion} >> CU charge, where CU is the

capacitance – built-in voltage product. Nevertheless, experimentally much higher charges are almost always obtained than this limit, which is also not fully understood yet. We therefore refer to the density obtained in BACE to the "apparent density" in the device that is obtained by integrating the extracted current and dividing the result by e*Vol. The externally extracted densities (as obtained by integrating the external current) and listed in Table S2 should therefore be regarded as "apparent", or "relative" densities rather than exact stored ion densities (see also ref.[22]). Overall, despite uncertainties in the exact mobile ion density, both measurements confirm the significant increase in the ion density during aging in the mixed halide system, which is remarkably suppressed in the pure iodine system (Fig. 3H).

Supplementary Note S3.

Our recent DD simulations showed that taking the absolute value of the capacitance and the depletion layer, rather than the accumulation (Debye) layer approximation, can provide reliable mobile ion densities in the absence of a transport layer, although it would significantly underestimate the density in the case of complete devices with transport layers.[19] Even when disregarding the transport layers, the obtained densities indicate extremely high values comparable to the unit cell density ~10^{21} cm^{-3} in the case of the degraded mixed halide device, which is highly unlikely.

The equation for the capacitance of a depletion layer is:

$$C_{\mathrm{dep}}(V_{\mathrm{app}}) = \left[\frac{e\,\varepsilon\,\varepsilon_0\,n_{\mathrm{ion}}}{V_{\mathrm{bi}} + V_{\mathrm{th}} - V_{\mathrm{app}}}\right]^{1/2}$$

with

$$V_{\mathrm{th}} = \frac{k_{\mathrm{B}}T}{e}$$

where C is the low-frequency (quasi-static) areal capacitance in the depletion-plateau region, $\varepsilon$is the relative dielectric constant, ε_0 is the vacuum permittivity, e is the elementary charge, k_{B} is the Boltzmann constant, T is the measurement temperature, V_{bi} is the built-in potential, and $V_{\mathrm{app}}$is the applied bias.

Supplementary Note S4.

We follow the linear-decay extrapolation approach under MPPT.[9] The normalized efficiency retention under MPPT is defined as

$$R(t) = \frac{\mathrm{PCE}(t)}{\mathrm{PCE}(t_0)}$$

where t is the elapsed time since the start of the MPPT test, and t_0 denotes the initial time point used for normalization. The projected T80 is estimated from the average retention at the last measured time (t_1) according to

$$\mathrm{T80} = t_1 + \frac{R(t_1) - 0.8}{k}$$

We note that the overall retention appears to flatten out, therefore, the linear approximation is considered to be a conservative estimate.

Supplementary References

1 S. Goedecker, M. Teter and J. Hutter, *Phys. Rev. B*, 1996, **54**, 1703–1710.
2 J. VandeVondele and J. Hutter, *J. Chem. Phys.*, 2007, **127**, 114105.
3 S. Nosé, *J. Chem. Phys.*, 1984, **81**, 511–519.
4 G. Kresse and J. Furthmüller, *Comput. Mater. Sci.*, 1996, **6**, 15–50.
5 G. Kresse and J. Furthmüller, *Phys. Rev. B*, 1996, **54**, 11169–11186.
6 J. P. Perdew, K. Burke and M. Ernzerhof, *Phys. Rev. Lett.*, 1996, **77**, 3865–3868.
7 G. Henkelman, B. P. Uberuaga and H. Jónsson, *J. Chem. Phys.*, 2000, **113**, 9901–9904.
8 K. Momma and F. Izumi, *J. Appl. Crystallogr.*, 2011, **44**, 1272–1276.
9 Z. Dong, J. Hu, X. Guo, Z. Shi, H. Chen, Y. Wang, R. Luo, J. A. Steele, Z. Degnan, E. Solano, Q. Zhou, N. Kalasariya, N. Li, T. Wang, J. Chen, L. K. Lee, Y. Wang, J. Li, M. Stolterfoht, M. Sui, Y. Lu and Y. Hou, *Nat. Mater.*, DOI:10.1038/s41563-025-02375-8.
10 J. Zhang, N. Yan, Y. Cao, Y. Li, R. Wang, D. Qi, J. Pi, N. Li, X. Feng, J. Wu, X. Liu, X. Gao, Y. Liu, S. (Frank) Liu and J. Feng, *Adv. Mater.*, 2025, e11162.
11 Y. Song, X. Cai, H. Ge, X. Liu, Z. Liu, A. Li, N. Shibayama and X.-F. Wang, *Energy Environ. Sci.*, 2026, 10.1039.D5EE05252A.
12 C. M. Wolff, L. Canil, C. Rehermann, N. Ngoc Linh, F. Zu, M. Ralaiarisoa, P. Caprioglio, L. Fiedler, M. Stolterfoht, S. Kogikoski, I. Bald, N. Koch, E. L. Unger, T. Dittrich, A. Abate and D. Neher, *ACS Nano*, 2020, **14**, 1445–1456.
13 J. Shen, X. Ge, Q. Ge, N. Li, Y. Wang, X. Liu, J. Tao, T. He and S. Yang, *ACS Appl. Mater. Interfaces*, 2024, **16**, 24748–24759.
14 J. Chen, D. Wang, S. Chen, H. Hu, Y. Li, Y. Huang, Z. Zhang, Z. Jiang, J. Xu, X. Sun, S. K. So, Y. Peng, X. Wang, X. Zhu and B. Xu, *ACS Appl. Mater. Interfaces*, 2022, **14**, 43246–43256.
15 W. Chai, L. Li, W. Zhu, D. Chen, L. Zhou, H. Xi, J. Zhang, C. Zhang and Y. Hao,

Research, 2023, **6**, 0196.

16 S. Zhou, B. M. Gallant, J. Zhang, Y. Shi, J. Smith, J. N. Drysdale, P. Therdkatanyuphong, M. Taddei, D. P. McCarthy, S. Barlow, R. C. Kilbride, A. Dasgupta, A. R. Marshall, J. Wang, D. J. Kubicki, D. S. Ginger, S. R. Marder and H. J. Snaith, *J. Am. Chem. Soc.*, 2024, **146**, 27405–27416.

17 X. Zhao, T. Liu, Q. C. Burlingame, T. Liu, R. Holley, G. Cheng, N. Yao, F. Gao and Y.-L. Loo, *Science*, 2022, **377**, 307–310.

18 D. A. Jacobs, H. Shen, F. Pfeffer, J. Peng, T. P. White, F. J. Beck and K. R. Catchpole, *J. Appl. Phys.*, 2018, **124**, 225702.

19 J. Diekmann, F. Peña-Camargo, N. Tokmoldin, J. Thiesbrummel, J. Warby, E. Gutierrez-Partida, S. Shah, D. Neher and M. Stolterfoht, *J. Phys. Chem. Lett.*, 2023, **14**, 4200–4210.

20 D. A. Jacobs, H. Shen, F. Pfeffer, J. Peng, T. P. White, F. J. Beck and K. R. Catchpole, *J. Appl. Phys.*, 2018, **124**, 225702.

21 D. Moia, I. Gelmetti, P. Calado, W. Fisher, M. Stringer, O. Game, Y. Hu, P. Docampo, D. Lidzey, E. Palomares, J. Nelson and P. R. F. Barnes, *Energy Environ. Sci.*, 2019, **12**, 1296–1308.

22 J. Thiesbrummel, S. Shah, E. Gutierrez-Partida, F. Zu, F. Peña-Camargo, S. Zeiske, J. Diekmann, F. Ye, K. P. Peters, K. O. Brinkmann, P. Caprioglio, A. Dasgupta, S. Seo, F. A. Adeleye, J. Warby, Q. Jeangros, F. Lang, S. Zhang, S. Albrecht, T. Riedl, A. Armin, D. Neher, N. Koch, Y. Wu, V. M. Le Corre, H. Snaith and M. Stolterfoht, *Nat. Energy*, 2024, **9**, 664–676.